



Publication Year	2018
Acceptance in OA	2020-10-20T13:47:31Z
Title	Thermal Stability of Water Ice in Ceres' Craters: The Case of Juling Crater
Authors	FORMISANO, Michelangelo, Federico, C., DE SANCTIS, MARIA CRISTINA, FRIGERI, ALESSANDRO, Magni, G., RAPONI, Andrea, TOSI, Federico
Publisher's version (DOI)	10.1029/2017JE005417
Handle	http://hdl.handle.net/20.500.12386/27898
Journal	JOURNAL OF GEOPHYSICAL RESEARCH (PLANETS)
Volume	123

RESEARCH ARTICLE

10.1029/2017JE005417

Special Section:

Ice on Ceres

Key Points:

- Ice stability on the surface of the crater Juling is an issue closely related to the Herschel observations of water vapor around Ceres.
- We apply a 3-D thermophysical model with real topography in order to evaluate the surface temperatures and the ice sublimation rates
- Juling northern wall, due to its faint solar illumination, results to be a good place to host water ice

Supporting Information:

- Supporting Information S1
- Data Set S1

Correspondence to:

M. Formisano,
michelangelo.formisano@iaps.inaf.it

Citation:

Formisano, M., Federico, C., De Sanctis, M. C., Frigeri, A., Magni, G., Raponi, A., & Tosi, F. (2018). Thermal stability of water ice in Ceres' craters: The case of Juling crater. *Journal of Geophysical Research: Planets*, 123, 2445–2463. <https://doi.org/10.1029/2017JE005417>

Received 11 AUG 2017

Accepted 6 AUG 2018

Accepted article online 14 AUG 2018

Published online 27 SEP 2018

Thermal Stability of Water Ice in Ceres' Craters: The Case of Juling Crater

M. Formisano¹ , C. Federico¹, M. C. De Sanctis¹ , A. Frigeri¹ , G. Magni¹, A. Raponi¹ , and F. Tosi¹ 

¹Istituto di Astrofisica e Planetologia Spaziali, INAF, Rome, Italy

Abstract Ice thermal stability on the surface of the dwarf planet Ceres is an important issue linked to the Herschel observations of water vapor around Ceres. One of these surficial ice deposits is located within the 20-km crater Juling (35°S, 168°E). The study of water ice exposure in this specific crater is particularly interesting because it has been observed that the water ice abundance changes on a time scale of a few months. To understand the ice behavior, we applied a 3-D finite element method thermophysical model to the study of Juling crater in order to determine the water ice sublimation rate. We use a detailed shape model of Ceres derived from optical imagery returned by the Framing Camera on board Dawn. We explore the effects of different heliocentric distances and different thermal inertia values, comparing our numerical predictions with the observational evidences returned by VIR and by the Herschel Space Observatory.

Plain Language Summary Ceres is a dwarf planet of the solar system with a significant amount of water both in its interior and in the surface layers. A crater in the southern hemisphere, Juling, is characterized by the presence on its surface of a mixture of ice and rocks as revealed by recent VIR data from the Dawn spacecraft. This crater is a good place to preserve ice since it is poorly illuminated, particularly in the northern wall. Most important is the detection of ice variations on its wall during the Dawn visible and infrared mapping spectrometer observations. In this work we performed numerical simulations in order to evaluate temperatures and water ice sublimation rate, assuming reasonable values for the physical parameters, and to estimate the longevity of ice on the surface of Ceres.

1. Introduction

There is considerable evidence to interpret Ceres as a world with a huge presence of water ice. First of all, its relatively low bulk density, that is, 2,162 kg m⁻³ (Park et al., 2016; Russell et al., 2016), suggests the presence of a low density material that can be identified in water ice. Even before the Dawn observations, numerical models suggested the presence of water ice in a percentage between 17% and 27% by mass, fractionated between the silicate core and the mantle (e.g., Castillo-Rogez & McCord, 2010; McCord & Sotin, 2005). In some models of the internal structure of Ceres, the mantle has been considered as made of pure ice (Castillo-Rogez, 2011; McCord & Sotin, 2005; Neveu et al., 2015), while in others, as a mixture of silicates and organics (Castillo-Rogez & McCord, 2010) or chondritic rock (Neveu & Desch, 2015). All these models are based on the idea that Ceres has a differentiated structure. Alternatively, Zolotov (2017) has assumed that Ceres is an undifferentiated object. However, the value of the inferred normalized mean moment of inertia (0.37; Park et al., 2016) suggests that Ceres is at least partially differentiated. The quantity of water ice is a crucial parameter in the stability of the crust and affects its possible overturn with consequent chemical reprocessing of the crust itself as discussed in Formisano, Federico, et al. (2016). Recently, Bland et al. (2016), analyzing craters morphology, suggested the presence of water ice in percentage between 30% and 40% in the shallow subsurface, while Fu et al. (2017), by using a viscoelastoplastic finite-element model, estimated an upper limit of 25%. The Ceres mineralogy indicates a pervasive alteration by liquid water (Carrozzo et al., 2018; De Sanctis et al., 2015, 2016; Raponi et al., 2017). An aqueous origin for ammonium salts (NH₄HCO₃ and NH₄Cl) observed in the bright spots inside Occator (20°N, 238°E; De Sanctis et al., 2016; Raponi et al., 2017) has been proposed by Zolotov (2017). Finally, visible and infrared mapping spectrometer (VIR) (De Sanctis et al., 2011) data have recently revealed water ice-rich areas in different localized regions (Combe et al., 2016; Raponi et al., 2017, 2018), among these of particular interests are Juling (35°S, 168°E) and Oxo (42°N, 359°E). Occator crater, which is characterized by a bright sodium-carbonate rich unit (De Sanctis et al., 2016;

Raponi et al., 2017), seems to show potential activity (haze; Nathues et al., 2015), even if this evidence is contested in literature (Schorghofer et al., 2016). In general, many areas show morphological evidences for ground ice (Schmidt et al., 2017) while other areas, which do not currently show water ice evidences, are likely the result of an intense hydrothermal process that gave rise to highly fluidized material/impact melt (Tosi et al., 2017).

The discovery of widespread ammoniated phyllosilicates on Ceres' surface (De Sanctis et al., 2015) suggests that Ceres' formation might have occurred in the outer solar system or that Ceres was formed in its current position and subsequently incorporated abundant material coming from colder regions of the solar system (De Sanctis et al., 2015). In the first case, after the accretion through icy planetesimal collisions, Ceres might have migrated to its current position (McKinnon, 2008, and references therein). In the second case, abundant volatile ices should have been incorporated during its accretion. However, as pointed out by Marchi et al. (2016), the lack of large craters (100–400 km size) does not seem compatible with a late implantation of Ceres in the main belt.

Herschel observations of water vapor around Ceres (6 kg s^{-1} ; Küppers et al., 2014) have revealed the possible activation of ice-rich areas. Even before Herschel observations, A'Hearn and Feldman (1992) presented observations of the hydroxyl, a product of the photo-dissociation of the water, showing a variability of the amount of water. Afterward, ultraviolet observations (Roth et al., 2016) by using the Cosmic Origin Spectrograph provided an upper limit on water vapor rate compatible with previous measurements. The fact that different measurements converge to a similar value (6 kg s^{-1}) leads to speculate that the source is unique or reproducible in time. Several mechanisms have been proposed to explain this water ice activity. A'Hearn and Feldman (1992) proposed as source of this emission a northern cap of frost, which sublimated during the summer after having been accumulated during the winter, as already discussed by Fanale and Salvail (1989). This cometary-type emission is also investigated by Formisano, De Sanctis, et al. (2016). Cryovolcanism is another possible mechanism (Neveu & Desch, 2015): liquid water in the interior can freeze and overpressurizes the remaining liquid reservoir driving a cryovolcanic flow. Evidence of cryovolcanism is suggested by landforms on the Ceres' surface, identifiable as viscous cryovolcanic domes (Ruesch et al., 2016). Water ice-rich (target or impactor) impacts (A'Hearn & Feldman, 1992), energetic solar flares (Villarreal et al., 2017), gravitational overturn of the crust (Formisano, Federico, et al., 2016) are other possible explanations. Water vapor emitted could contribute to the formation of a transient atmosphere, as discussed by Formisano, Federico, et al. (2016), who investigated the typical timescale of an optically thin transient atmospheric envelope applying a smoothing particle hydrodynamic code. This transient atmosphere could be generated by an impact on an icy patch on the surface or by some kind of abrupt discontinuity of the surface. A typical timescale found in Formisano, Federico, et al. (2016) is only few days, longer than the estimation (7 hr) of Schorghofer et al. (2016). A transient atmosphere can also be generated assuming that the activation process is due to solar energetic protons, whose energy is sufficient to sputtering water ice in the first layers below the surface (Villarreal et al., 2017).

The estimation of the stability time of water ice on the surface or in the shallow subsurface is strictly linked to the most plausible exposure mechanism. Fanale and Salvail (1989) found that ice could have survived for a time compatible with the solar system age at 10–100 m depths near the equator, and 1–10 m depths at latitudes $>40^\circ$. Hayne and Aharonson (2015) proposed that water ice may be stable for $>1 \text{ Myr}$ at a latitude $>60^\circ$ and in case of high thermal inertia. Conversely, at low latitudes $<30^\circ$ and in case of low thermal inertia the stability is ensured for a timespan $<1,000 \text{ years}$. Titus (2015) found that cometary-type emission is unlikely at low latitudes, due to the instability of the near-surface ice, while the ice is stable, for a reasonable range of physical parameters (thermal inertia, roughness of the surface and slope) at midlatitudes (40° – 60°). In Formisano, De Sanctis, et al. (2016) it has been showed that the surface ice is stable for very few orbits at low latitudes and the matching with Herschel measurements (Küppers et al., 2014) is met considering a 100-km emitting area, placed at a depth compatible with the skin depth. Schorghofer et al. (2016) pointed out how some regions of the surface of Ceres can be permanently in shadow due to small spin axis tilt (4°). In this case, they estimated that the total region in shadow in the northern hemisphere is equal to $1,800 \text{ km}^2$, using the topography obtained from stereo imaging by the Dawn spacecraft. These regions could trap water ice over geological time scales. Prettyman et al. (2017), using nuclear spectroscopy data acquired by the Dawn mission, showed that the regolith contains high concentrations of hydrogen at mid-high latitudes, consistent with the presence of widespread water ice not far from the surface also at midlatitudes. This evidence supports the theoretical predictions according to which ice can be stable for a very long time (billions of year) within a meter beneath the surface. More recently, Landis et al. (2017) explored different configurations of water ice

Table 1
Scenarios We Developed in This Study

Scenario	Distance (AU)	Solar constant (Wm^{-2})	Subsolar point latitude ($^{\circ}$)	Thermal inertia (TIU)	Note
A1	2.90	163	0.471	500	Exposed ice
A2	2.90	163	0.471	50	Exposed ice
B1	2.55 (perihelion)	210	-2.98	500	Exposed ice
B2	2.55 (perihelion)	210	-2.98	50	Exposed ice
C	2.71	186	-2.2	50	Exposed ice
D	2.71	186	-2.2	50	1 cm buried ice

(global buried pore-filling ice, global buried excess ice and local exposed surface ice) for Ceres. An agreement within few terrestrial years of their results with the Herschel observations (Küppers et al., 2014) is obtained in case of surface ice optically bright, or for a shorter timespan depending on the contamination of the regolith in the ice patches.

In this work, we developed a 3-D finite element method (FEM) model in order to calculate the temperature distribution on the Ceres' surface using the shape model of Ceres, based on the images acquired by the Dawn's Framing Camera (Sierks et al., 2011) during the Survey mission phase (Preusker et al., 2016). In particular, we focused on Juling crater because it exhibits spectral evidence of water ice variation in its northern wall (Raponi et al., 2018). This ice on the wall covers an area of about 40 km^2 , and it is almost permanently in shadow. From the analysis of VIR observations along 6 months, Raponi et al. (2018) found evidence of an increase of water ice from $9.1 \pm 0.3\%$ to $13.7 \pm 0.9\%$ of the total area of the crater wall, being the first observation acquired at 2.961 AU and the last one at 2.876 AU. Raponi et al. (2018) suggest we are observing the increasing part of a seasonal cycle. Our simulations evaluate the surface temperatures and the consequent rate of the water emission, exploring different values of heliocentric distances and thermal inertia.

2. Scenarios

We have developed several cases characterized by a different heliocentric distance in order to explore how the surface temperatures and ice sublimation rate are affected by the seasons. In Table 1 we have summarized all the cases under investigation. For cases A and B we have also tested two different values of thermal inertia, 50 and 500 TIU. This choice is strictly linked to the thermodynamic parameters assumption and a detailed discussion will be reported in the following section 3 "The Model".

The main model in this work is represented by the case A characterized by an heliocentric distance compatible with the one to which observations reported in Raponi et al. (2018) took place. For this case we will report the illumination condition (x - y plane) and the 3-D surface temperature. In case B we investigated the temperatures and the sublimation rate at perihelion, focusing only on the "icy region", the northern wall of the crater containing ice, whose characteristic will be explained later. We also analyzed the water vapor flux at Herschel distance measurements (Küppers et al., 2014), that is, 2.71 AU. This distance corresponds to the detection of Herschel of 24 October 2012 (Küppers et al., 2014): no significant variations in the results are obtained if we use the heliocentric distance at which the observations occurred 2 weeks before, that is, 2.72 AU (Küppers et al., 2014). The case at Herschel heliocentric distance has been investigated in two different configurations of the hypothesized structure, in the first one the ice is placed directly on the surface (case C), in the second one it is buried at 1 cm below a diffusive boundary (case D). Furthermore, an estimation of the ice sublimation rate at given points along the orbit is also provided.

3. The Model

3.1. General Description

Since we study the surface and subsurface temperatures of Ceres, the energy input is provided by the Sun: part of this energy is conducted into the near-surface, another part is irradiated back into the open space and the rest is used to sublimate the ice, as shown in Figure 1. Self heating, between the different facets of the shape model, is included in our modeling.

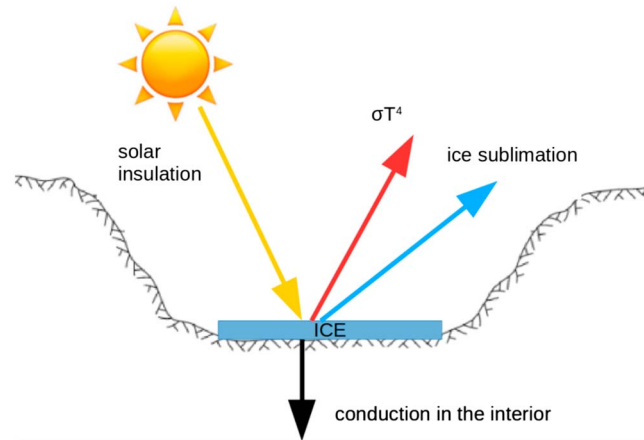


Figure 1. Energy balance on Ceres' surface.

The shallow subsurface of Ceres contains ice and a mixture of silicates, salts and in general such kind of mixture is characterized by values of thermal inertia that do not allow deep penetration of the thermal wave for the known value of the rotational period, that is, 9.07 hr (Chamberlain et al., 2007).

The diurnal skin depth, whose definition is

$$S_d = \sqrt{\frac{PK}{\pi\rho c_p}}, \quad (1)$$

where P is the rotational period, K the thermal conductivity, c_p the specific heat and ρ the density, is 4 mm with a thermal inertia of 50 TIU (cases A2–B2) or 4 cm with a thermal inertia of 500 TIU (cases A1–B1). The values obtained for the skin depth are the reason why we look to the depth distribution of the induced temperatures only for few centimeters. We recall that the thermal inertia is defined as $\sqrt{K\rho c_p}$ and measures the resistance of material to the temperature change.

We adopted a 3-D FEM code by using the COMSOL Multiphysics software (www.comsol.com). The module used is the “Heat Transfer in Solids.” The heat transfer is computed solving the classical heat equation with a source, $Q(r, T)$, which represents the energy absorbed from the solid matrix due to the sublimation process (Capria et al., 1996; De Sanctis, Lasue, & Capria, 2010; De Sanctis, Lasue, Capria, Magni, et al., 2010; Espinasse et al., 1991; Formisano, De Sanctis, et al., 2016; Lasue et al., 2008):

$$\rho(r)c_p(r, T)\frac{\partial T}{\partial t} = \vec{\nabla} \cdot (K(r, T)\vec{\nabla}T) + Q(r, T) \quad (2)$$

where T is the temperature and t the time. Thermal convection is negligible since we are interested only to surface and subsurface temperatures. Water vapor emission is treated by using the mass conservation equation:

$$\frac{\partial \rho}{\partial t} = -\vec{\nabla} \cdot \vec{J} + \tilde{Q}(r, T), \quad (3)$$

where $\tilde{Q}(r, T)$ is the gas source term due to sublimation process. In a quasi-stationary regime, we can write the \vec{J} diffusion flux vector as

$$\vec{J} = -D\vec{\nabla}p, \quad (4)$$

where p is the partial pressure of the water vapor and D is the gas diffusion coefficient. This equation derives from the Darcy's law:

$$J \propto \frac{1}{\nu}\nabla p, \quad (5)$$

where ν is the kinematic viscosity of the fluid, an experimental formulation found for fluid flow through a porous medium.

The diffusion coefficient is calculated according to the kinetic theory of gases, by evaluating the Knudsen number, a dimensionless parameter defined as

$$K_n = \frac{\lambda}{2r_p}, \quad (6)$$

where r_p is the pore radius and λ is the mean free path, defined as (Fanale & Salvail, 1987)

$$\lambda = \frac{\mu}{\sqrt{2}\pi d^2 \rho N_a}, \quad (7)$$

where μ is the water molar mass (0.018 kg per mole), d is the water molecular diameter, ρ is the density of the water vapor and N_a is the Avogadro's number. Assuming $d = 5 \times 10^{-10}$ m (Espinasse et al., 1991), the mean free path is of the order of 10^{-1} m, so $K_n < 1$. This means that the collisions between molecules prevail and the escaping velocity of the gas is of the order of the mean thermal velocity:

$$v = \sqrt{\frac{8RT}{\pi\mu}}. \quad (8)$$

We can compare this escaping velocity with the sound velocity, whose definition (in the regime of ideal gases) is

$$v_s = \sqrt{\frac{\gamma RT}{\mu}}, \quad (9)$$

where γ is the adiabatic index set at 1.7. The ratio between v and v_s defines in fluid dynamics the Mach number, a dimensionless quantity which is used to determine if the approximation of incompressible fluid is valid. For Mach number > 1 , compressibility effects become important and the density changes faster than the velocity changes: this is the so called supersonic regime. This will not affect the local thermodynamic equilibrium that we will assume in the sublimation rate calculation, since the supersonic regime characterizes only the last acceleration phase of the evaporation process, when the density drops down and the mean free path of the gas molecules goes to infinity.

In such regime, the diffusion coefficient D is defined as

$$D = \frac{r_p^2 p}{8vKT N_a}, \quad (10)$$

where $r_p = 10^{-4}$ m (see, e.g., De Sanctis, Lasue, & Capria, 2010). Using equation (4) we can write the equation (3) as

$$\frac{\partial \rho}{\partial t} = \vec{\nabla} \cdot (D \vec{\nabla} p) + \tilde{Q}(r, T). \quad (11)$$

From equation (11) we can obtain an expression for $\tilde{Q}(r, T)$ by assuming that the water vapor acts like a perfect gas:

$$\tilde{Q}(r, T) = \frac{1}{R_{spec} T} \frac{\partial p}{\partial t} - \vec{\nabla} \cdot (D \vec{\nabla} p), \quad (12)$$

where R_{spec} is the specific gas constant defined as the ratio between the universal gas constant (R) and the molar mass (μ). This last term ($\tilde{Q}(r, T)$) is linked to the gas source term (Q) of the heat equation (see equation (2)), since sublimation subtracts energy in a quantity directly proportional to the latent heat of sublimation:

$$Q(r, T) = -\phi L(T) \tilde{Q}(r, T), \quad (13)$$

where ϕ is the porosity and $L(T)$ is the latent heat of sublimation. Finally, using equations (12) and (13) we can write the heat equation (2) in the form:

$$\left(\rho c + \frac{\phi H(T)}{RT} \frac{\partial p_{sat}(T)}{\partial T} \right) \frac{\partial T}{\partial t} = \quad (14)$$

$$\vec{\nabla} \cdot (K(T) \vec{\nabla} T) + \phi L(T) \vec{\nabla} \cdot (D(T) \vec{\nabla} p_{sat}), \quad (15)$$

Table 2
Physical Parameters Used in This Study

	Symbol	Value	Reference
General parameters			
Solar constant at Earth distance	S	$1,361 \text{ W m}^{-2}$	—
Rotational Period	τ	9.074 hr	Russell et al. (2016)
Porosity	ϕ	0.5	This study
Initial temperature	T_0	160 K	This study
Regolith parameters			
Volumetric concentration	vf_{reg}	0.90	Raponi et al. (2018)
Albedo	a_{reg}	0.03	Ciarniello et al. (2017) Li et al. (2016)
Density	ρ_{reg}	$1,600 \text{ kg m}^{-3}$	Heiken et al. (1991)
Specific heat	$c_{p,\text{reg}}$	$760 \text{ J kg}^{-1} \text{ K}^{-1}$	Heiken et al. (1991)
Thermal conductivity	K_{reg}	$2 \text{ W m}^{-1} \text{ K}^{-1}$	Heiken et al. (1991)
Ice parameters			
Volumetric concentration	vf_{ice}	0.10	Raponi et al. (2018)
Albedo	a_{ice}	0.06	Raponi et al. (2017) Ciarniello et al. (2017)
Density	ρ_{ice}	950 kg m^{-3}	—
Specific heat	$c_{p,\text{ice}}$	$7.037T + 185.0 \text{ J kg}^{-1} \text{ K}^{-1}$	Ellsworth and Schubert (1983)
Thermal conductivity	K_{ice}	$567/T \text{ W m}^{-1} \text{ K}^{-1}$	Klinger (1980)
Enthalpy of sublimation	$H(T)$	$51,983.9 - 20.0904T \text{ J mol}^{-1}$	Delsemme and Miller (1971)

where we have assumed valid the local thermodynamic equilibrium and so $Q(r, T)$ depends on the variation of the saturation pressure of the water vapor.

The physical quantities of the ice-rock mixture, with which we have modeled the surface, are weighted by volume (density and thermal conductivity) and by mass (specific heat), as follows:

$$\rho_{\text{mix}} = vf_{\text{ice}}\rho_{\text{ice}} + vf_{\text{reg}}\rho_{\text{reg}}, \quad (16)$$

$$K_{\text{mix}} = vf_{\text{ice}}K_{\text{ice}} + vf_{\text{reg}}K_{\text{reg}}, \quad (17)$$

$$c_{p,\text{mix}} = mf_{\text{ice}}c_{p,\text{ice}} + mf_{\text{reg}}c_{p,\text{reg}}, \quad (18)$$

where vf_{ice} and vf_{reg} are the volumetric percentage of ice and regolith (after porosity correction), while mf_{ice} and mf_{reg} are the mass percentages. Thermal conductivity is also corrected for the Hertz factor, which takes into account the effective contact area of the particles. The Hertz factor is defined as the ratio between the grain-to-grain area of contact and the cross section of the grain. It can strongly affect the thermal history of a planetary body as well as a cometary type objects since it can substantially modify the thermal conductivity (and so the thermal inertia) of such objects (Kossacki et al., 1994; Paton et al., 2010). The range of variability of this parameter is wide: from 0.1 to 10^{-4} , based on the KOSI (Kometensimulation) experiments (Huebner, 2006). In this work we tested two values, 10^{-1} and 10^{-3} , which together with the adopted values for K , ρ and c_p of the mixture rock-ice listed in Table 2 lead to thermal inertias of ≈ 500 TIU (cases A1 and B1 in Table 1) and ≈ 50 TIU (cases A2, B2, C, and D in Table 1). A value of 50 TIU for thermal inertia is in the middle of the range of the likely values found in literature 15 TIU (Spencer et al., 1989) to 80 TIU (Keihm et al., 2013; refer to Titus, 2015, for a detailed discussion about this issue). The uncertainty linked to this parameter is due both to the method/technique adopted in the calculation and to the Bond albedo used, as pointed by Rivkin et al. (2011). In order to evaluate the effects of the thermal inertia on the temperatures and the sublimation rate, we also investigated a value amplified by a factor 10, that is, 500 TIU. Note that values $>2,000$ TIU are not unusual for example in cemented regolith on Mars (Mellon et al., 2004), but these values lead to a flat day-night temperature profile, as shown in Figure 2 of Hayne and Aharonson (2015). Water ice saturation pressure is approximately defined as (Murphy & Koop, 2005)

$$p_{\text{sat}} = e^{\left(9.550426 - \frac{5723.265}{T} + 3.3068 \ln(T) - 0.00728332\right)}, \quad (19)$$

valid for $T > 110$ K. We have also tested different expressions for the saturation pressure, obtaining very similar results: see Murphy and Koop (2005) for a detailed review about vapor pressure parametrization and stated range of validity. The assumption of local thermodynamic equilibrium holds true if the characteristic time of gas transport is much longer than the characteristic time of sublimation process, so in this way the gas pressure is not affected by transport process (Koemle et al., 1992). As stated in Koemle et al. (1992), large deviations from the saturation pressure are expected only within a few pore radii distance from the sublimation surface. The ice sublimation rate is calculated through the classical expression of Delsemme and Miller (1971):

$$\Gamma = p_{sat} \sqrt{\frac{\mu}{2\pi RT}}, \quad (20)$$

whose units are $\text{kg m}^{-2} \text{s}^{-1}$. Equation (20) can be written in molecules $\text{m}^{-2} \text{s}^{-1}$ as

$$\Gamma^* = \frac{\Gamma Na}{\mu}, \quad (21)$$

where Na is the Avogadro's number.

Dividing the sublimation rate for the density of the ice (ρ_{ice}), we obtain the recession velocity of the ice:

$$v_{ice} = \frac{\Gamma}{\rho_{ice}}, \quad (22)$$

which is also the definition found in Landis et al. (2017).

3.2. Lifting of Dust Particles

When water ice sublimates, it can carry out dust particles and consequently make buried ice available for sublimation. We can estimate the critical size of the particles that can freely leave the surface of the crater by balancing the drag of the outflowing water vapor with the gravitational acceleration force and with the centrifugal acceleration contribution (Delsemme & Miller, 1971; Fanale & Salvail, 1984):

$$F_g - F_{drag} - F_{centr} = 0, \quad (23)$$

which can be written as

$$\frac{GMM_g}{R_C^2} - \pi a^2 v \Gamma - M_g R_C \omega^2 \cos^2 \theta = 0, \quad (24)$$

where M_g is the dust grain mass, M is the mass of Ceres, a is the size of the dust grain, v is the velocity of water vapor, R_C is the Ceres' mean radius, ω the angular velocity and θ the latitude of Juling. By substituting $M_g = (4/3)\pi \rho_{dust} a^3$ in the previous equation, we obtain

$$\frac{4\pi G M a^3 \rho_{reg}}{3R_C^2} - \pi a^2 v \Gamma - \frac{4\pi a^3 \rho_{reg} R_C \omega^2 \cos^2 \theta}{3} = 0, \quad (25)$$

and solving for a , we finally obtain (see, e.g., De Sanctis, Lasue, & Capria, 2010; Fanale & Salvail, 1984):

$$a = \frac{v \Gamma}{\frac{4\rho_{reg}}{3} \left(\frac{GM}{R_C^2} - R_C \omega^2 \cos^2 \theta \right)}. \quad (26)$$

Equation (26) gives the critical size (in meter) for the escaping dust grains: if the dust particles have a size greater than this critical value they are not blown off. Here we do not study the redeposition of the particles blown off: this is the matter of study of a next paper. In this equation the numerator represents the lifting force, which tends to raise the grains, against to the gravitational attraction, represented by the denominator. In Figure 2 a schematic view of the forces acting on a dust particle is represented. No sticking forces between the dust grains are taken into account (De Sanctis, Lasue, & Capria, 2010). It should be noted that this calculation is valid for flat surface: in case of crater rim, buried material could be exposed also by landslides. Regolith particle size distribution is discretized as a Gaussian distribution around the value of $100 \mu\text{m}$, which is the grain size modeled in Raponi et al. (2017), to which we refer the reader for the details on the methodology used to derive the grain size.

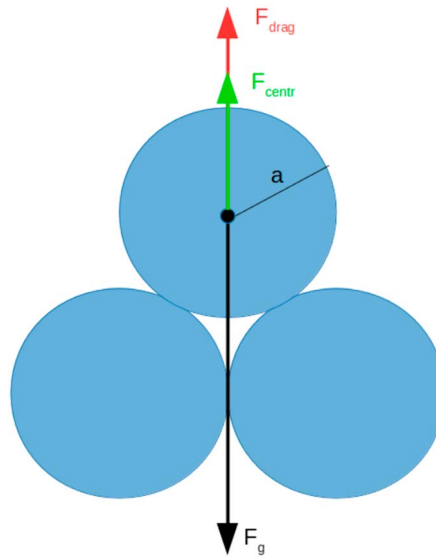


Figure 2. Forces acting on a stationary dust particle. If the particle size is greater than the critical value, it does not escape.

3.3. Initial and Boundary Conditions

The initial temperature of the Ceres' surface region where the Juling crater is located is set to 160 K, corresponding approximately to the radiation equilibrium temperature of Ceres at its average distance from the Sun. In order to achieve the stationary state, we performed 70 planetary rotations (Cerean days). On the surface a radiation boundary condition (σT^4) is imposed, while on the other sides (lateral and bottom) we imposed thermal insulation, which means zero heat flux.

The icy region, whose thermal evolution is to be studied, is located in the northern wall of the crater and has a surface of about 40 km² (Figure 3). Its composition has been determined to be a 10 vol.% of ice and 90 vol.% of rock (i.e., regolith; see Raponi et al., 2018), while in the rest of the surface, the percentage of ice is negligible. The bolometric albedo is calculated starting from the single scattering albedo (SSA) of the water ice and of the dark regolith, following Hapke (2012). The SSA of water ice is calculated from the optical constants (Clark et al., 2012; Hudgins et al., 1993) and assuming a grain size of 100 μm as derived by Raponi et al. (2018). The SSA of the dark regolith of Ceres has been derived by Ciarniello et al. (2017). Assuming 10% of surface covered by water ice, the bolometric albedo results to be 0.06. The albedo of regolith is assumed to be 0.03 (Ciarniello et al., 2017; Li et al., 2016).

All of the physical properties of regolith and ice are reported in Table 2.

3.4. Shape Model and Mesh

The shape model of Ceres has been derived on the basis of images acquired by the Framing Camera during the Survey mission phase (Preusker et al., 2016). In Figure 3A, we report the map of the Juling crater and in Figure 3B its 3-D reconstruction, obtained through the COMSOL Multiphysics software. Cartesian axes are displayed. In Figure 3B the blue area in the northern inner wall indicates the ice-rich region.

The Digital Terrain Model (DTM) used in our work was extracted from the Ceres' shape model (Preusker et al., 2016). The digital terrain data cover a longitude range from 166°35'25.26"E to 170°14'51.10"E and latitude from 34°8'1.16"S to 37°32'49.28"S. We processed the shape model data into a format and resolution suitable for the numerical code we have used. The original data have been processed and triangulated with an average size of 500 m, and converted in a stereolithography (STL) file, which has been ingested into the COMSOL software suite. The STL file is included in the supporting information.

The 3-D object we considered (see Figure 3B) has an approximated total area of 900 km², while the crater has an area of about 300 km². The "blue area" characterized by the presence of ice is about 40 km². The grid is made of triangular plates of varying size on the surface. Elements size of the numerical grid is automatically

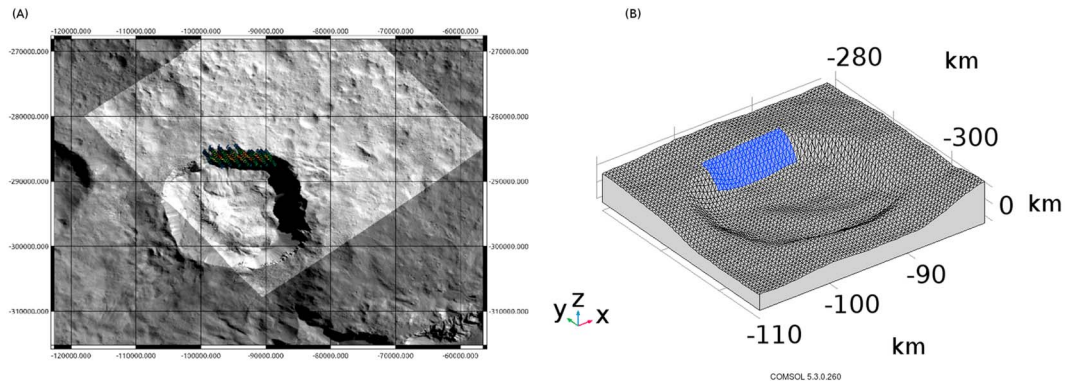


Figure 3. (a) Juling map based on the images acquired by the Framing Camera in the Dawn Survey Mission phase (Preusker et al., 2016); (b) 3-D reconstruction by COMSOL Multiphysics software. The blue area is approximately the region in which water has been detected by Raponi et al. (2018). Minus sign only indicates that Juling is located in the southern hemisphere.

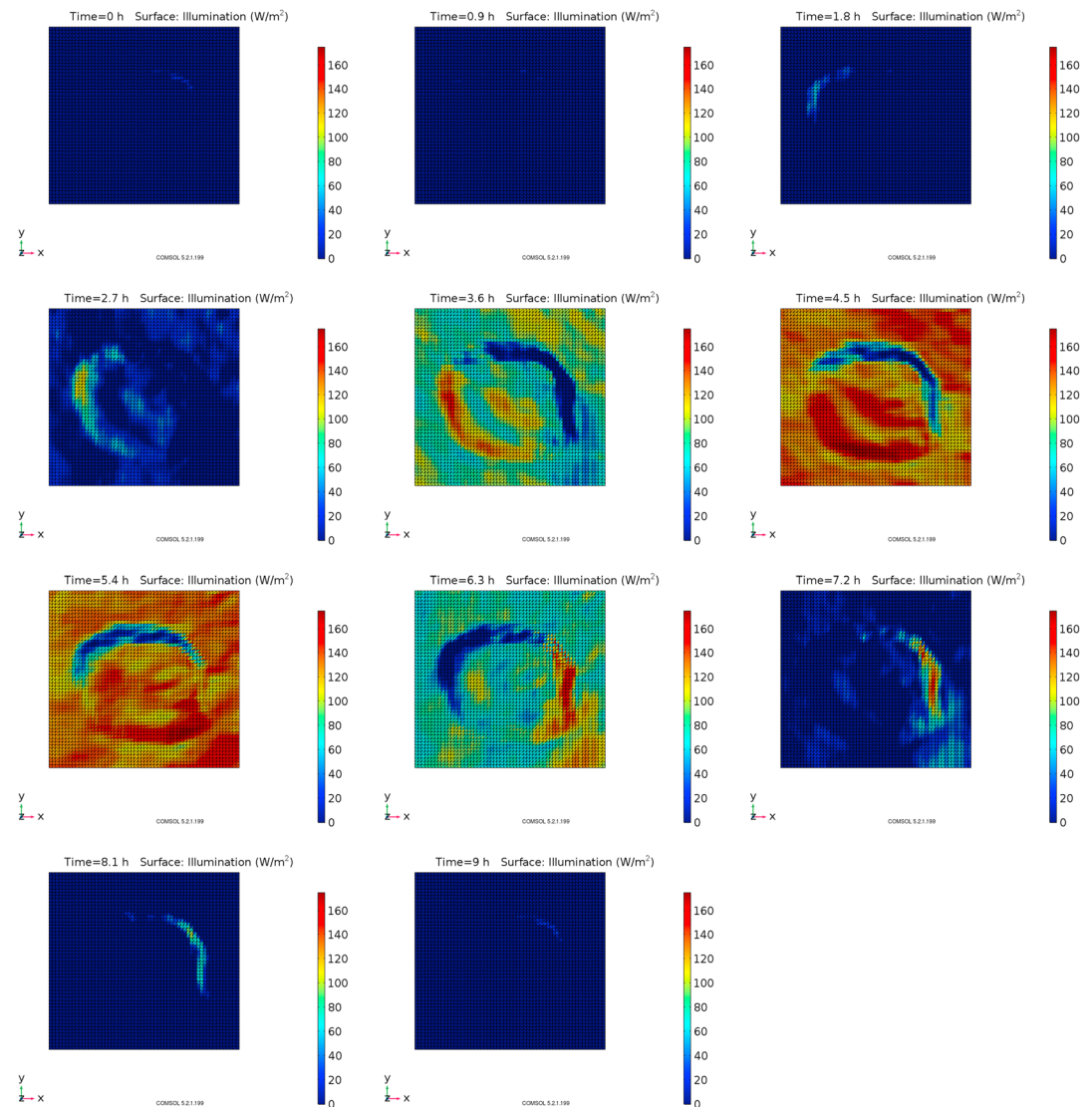


Figure 4. Surface illumination at 2.90 AU (cases A1 and A2) during a Cerean day with a time step \approx 1 hr.

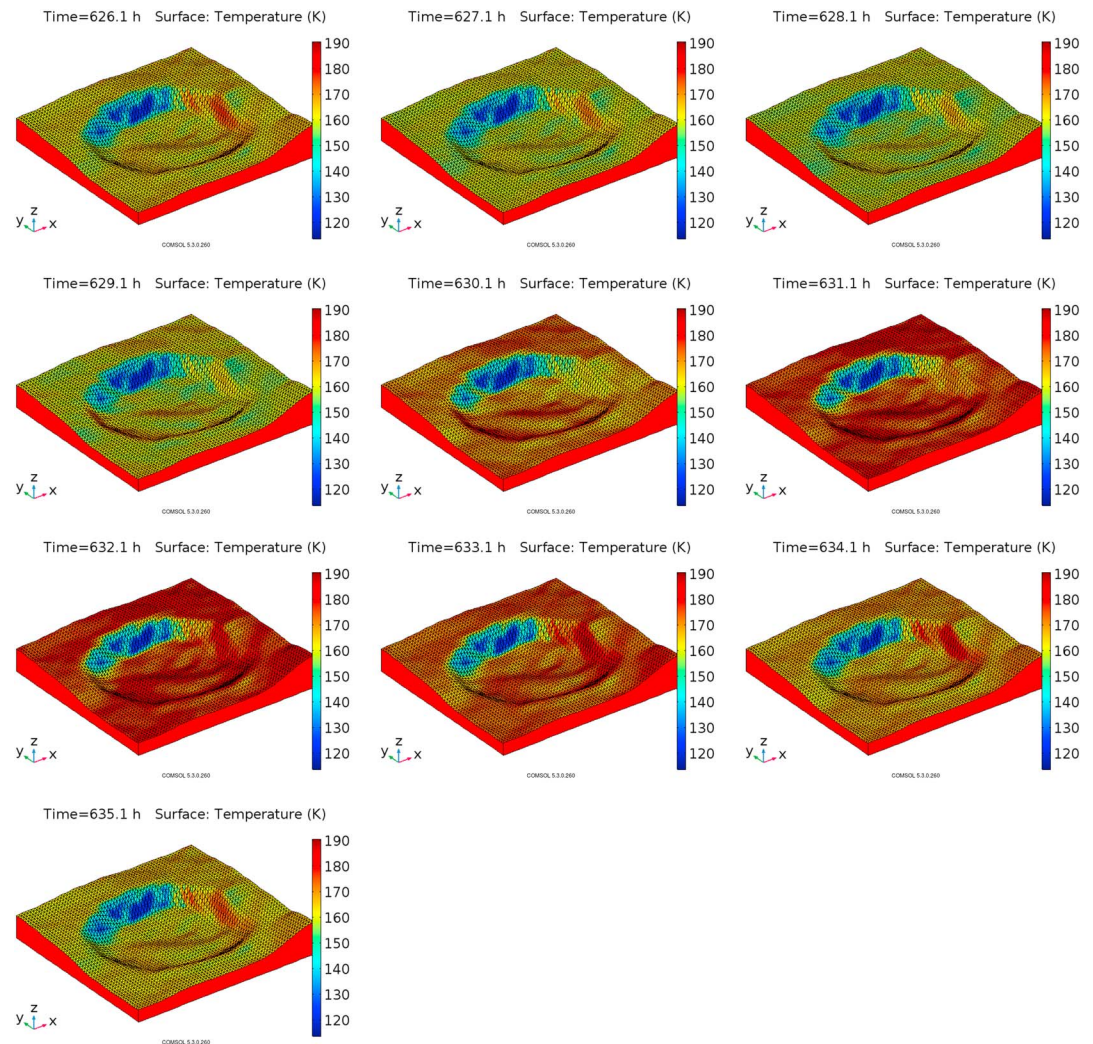


Figure 5. Case A1: 3-D temperature map at 2.90 AU, in case of thermal inertia of 500 TIU, during a Cerean day with a time step ≈ 1 hr. TIU = thermal inertia unit.

chosen by COMSOL Multiphysics calibrated for the physical equations involved in the numerical modeling. The minimum element's size is 0.116 km while the maximum size is 1.6 km. Free quadrilateral are used on the lateral sides of the 3-D reproduction of Juling, while on the bottom free triangles are used. The number of degrees of freedom is 75222 while the total number of elements of the grid is 138760.

3.5. Illumination Conditions

Before discussing the results obtained for the surface temperatures and water ice sublimation rate, we report in Figure 4 the illumination conditions of Juling crater at 2.90 AU. Once again, we remind that the only energetic input is provided by the Sun, so solar irradiance determines the surface temperatures and consequently the sublimation rates. In this figure we plot the solar irradiance with a time step of ≈ 1 hr, for a total time equal to the rotation period of the Ceres (≈ 9 hr). We observe that the icy region (northern wall of the crater) is always weakly illuminated compared to the other regions. This fact affects the ice sublimation rate and consequently the ice lifetime inside the crater.

The illumination on the shape model is computed by using the orbital parameters provided by the HORIZONS web interface (<https://ssd.jpl.nasa.gov/horizons.cgi>) and applying a rotational matrix along the z-axis of the shape model, which corresponds to the spin axis.

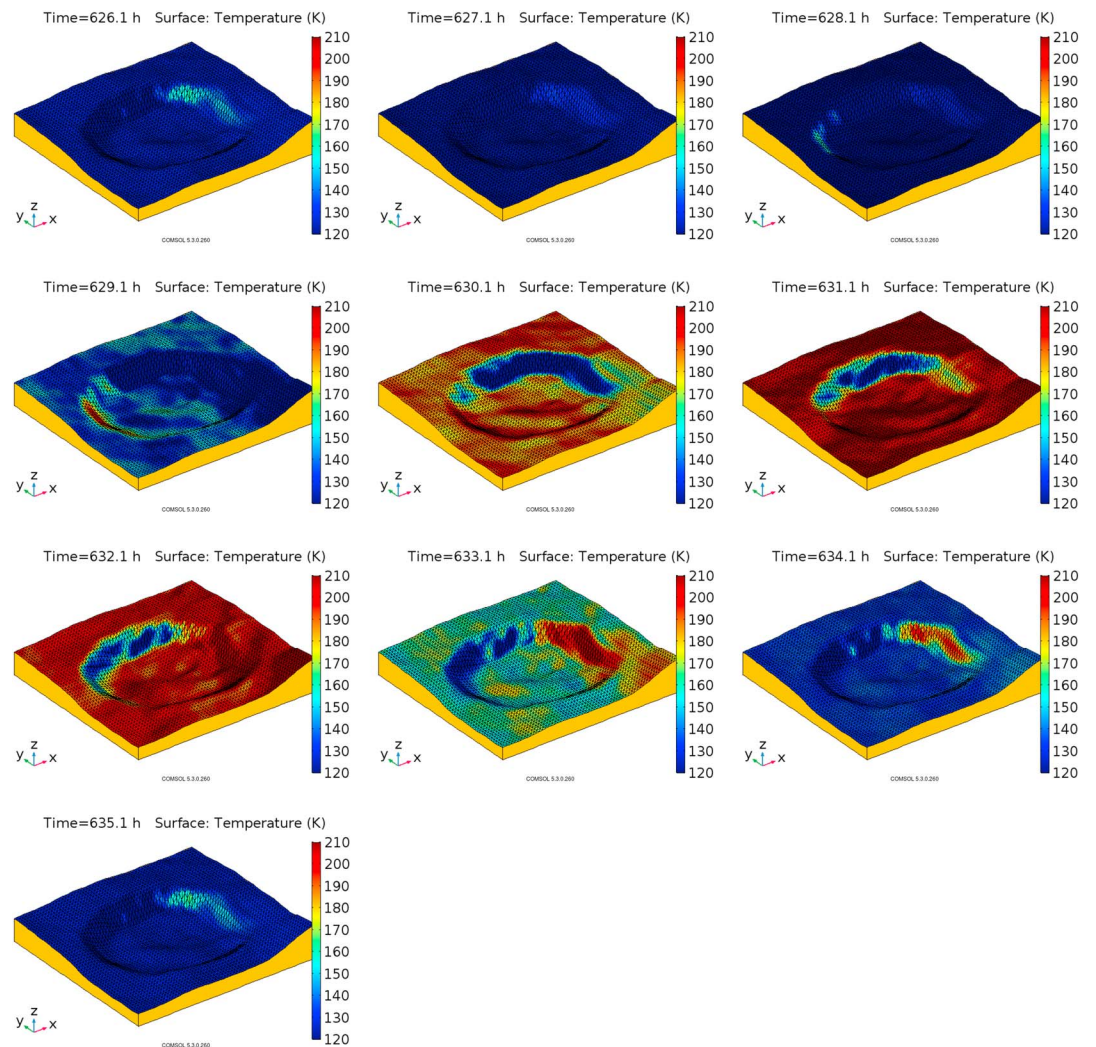


Figure 6. Case A2: 3-D temperature map at 2.90 AU, in case of thermal inertia of 50 TIU, during a Cerean day with a time step ≈ 1 hr. TIU = thermal inertia unit.

4. Results and Discussion

In this section we discuss the results obtained for the cases under investigation reported in Table 1. We evaluated in ≈ 70 Cerean days the necessary planetary rotations in order to achieve a stationary state. The procedure of integrating the model over a suitable number of Ceres rotations (about 70) to reach a quasi-equilibrium state is adopted in order to avoid excessively large CPU integration times. This relaxation phase has a timescale of about 30 Earth days, much lower than than the orbital period of Ceres, so that is assured a low variation of solar irradiation and surface temperature.

4.1. Cases A: 2.90 AU—VIR observations

In Figure 5 we report the surface temperature after about 70 planetary rotations when the stationary state is reached. Surface temperatures reflect the behavior of the illumination conditions and in all the studied regions, temperatures range from 120 K to 190 K. The icy region is characterized by a nearly constant temperature of about 140 K. Assuming an Hertz factor of 10^{-1} , the thermal inertia in the icy region is very high (≈ 500 TIU), as previously discussed. This case is labeled as A1. Using equations (20) and (22), we can calculate the maximum thickness of sublimated ice loss after one Ceres' rotation, resulting equal to 7.4×10^{-5} mm per Cerean day.

If we decrease by two orders of magnitude the Hertz factor, that is, 10^{-3} (case A2, see Figure 6), the surface reacts differently to the solar input, reaching a maximum temperature in the floor of the crater of about 210 K. In this case the thermal excursion is about 100 K. This different behavior is due to the low thermal inertia. If we

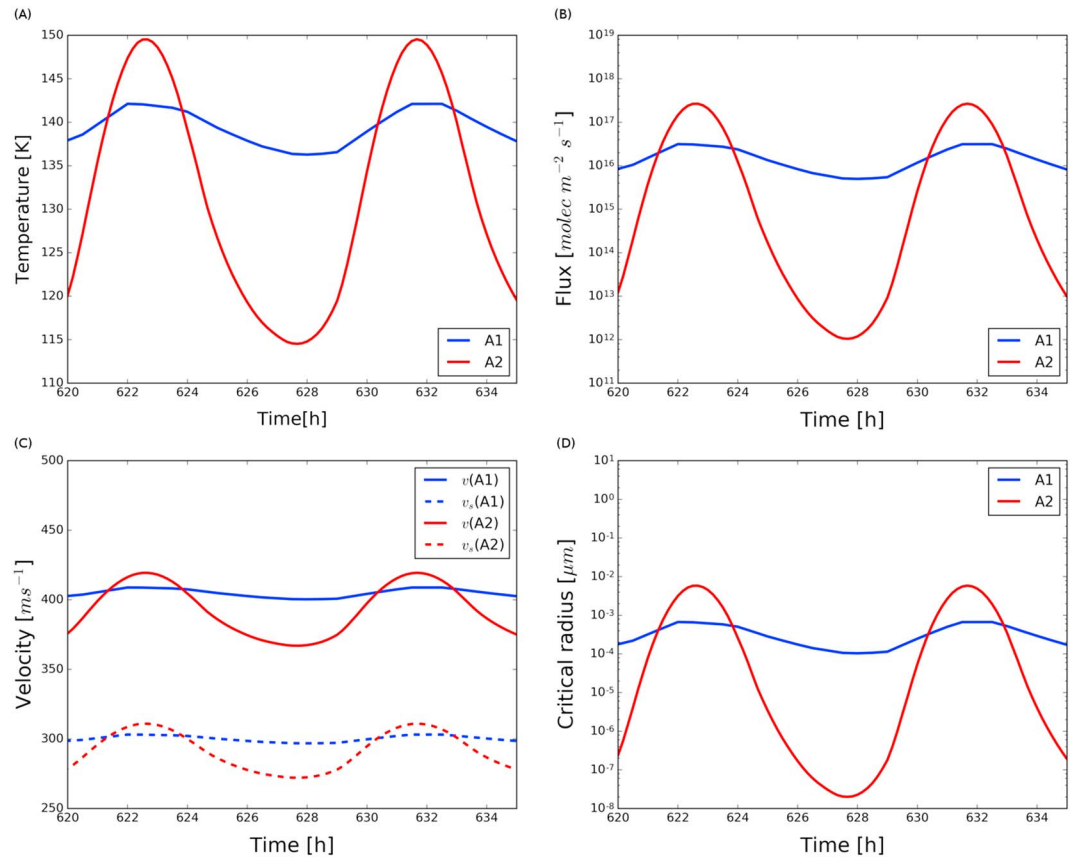


Figure 7. Characteristic behavior of the physical quantities for case A and for two different values of the thermal inertia: 500 TIU (case A1, blue line) and 50 TIU (case A2, red line): (a) Day-night temperatures of the icy region at 2.90 AU; (b) water flux in molecules $\text{m}^{-2} \text{s}^{-1}$; (c) velocity of the water vapor (v) and of the sound (v_s), where sound velocities are in dashed style; (d) critical radius for dust lifting.

calculate again the maximum sublimation rate using the equations (20) and (22) we obtain $\approx 2.7 \times 10^{-4}$ mm per Cerean day.

The effect of the Hertz factor on the thermal inertia and consequently on the “day-night” profile of the ice-rich region is clearly shown in Figure 7A, in which we report a typical Cerean day. When the thermal inertia is high (case A1), the temperature remains almost constant and its oscillations are confined within the day-night oscillations of the case A2 (low thermal inertia): such effect is also shown in the simulations of Hayne and Aharonson (2015). In case A2, the maximum value reached is ≈ 150 K. By comparing our temperatures with those of Hayne and Aharonson (2015), we note that the minimum and maximum values are consistent (see Figure 2 of Hayne & Aharonson, 2015). In Figure 7B we report the water flux in molecules $\text{m}^{-2} \text{s}^{-1}$. Extreme values are as high as 10^{17} molecules $\text{m}^{-2} \text{s}^{-1}$ in case A2 and about 10^{16} molecules $\text{m}^{-2} \text{s}^{-1}$ in A1. The trend of the flux versus time reflects the same behavior of the temperatures shown in Figure 7A. In Figure 7C we report the velocity of water vapor, which is the main thermal velocity of equation (8), for cases A1 and A2. We note that the escaping water velocity is always greater than the speed of sound, calculated according to equation (9), and the Mach number is > 1.3 , resulting in a supersonic regime.

Critical radius, in both cases, is very small because sublimation rate is not very strong with respect the gravity (see Figure 7d). For this reason, assuming a particle size of 100 μm , the dust eventually present above the icy patch is not removed by the sublimation of the water ice. This means that, unlike what generally happens to comets, the buried ice can not be exposed on the surface by the dust removal under these illumination conditions. It must be recall that we are not considering possible landslides that can expose icy surface.

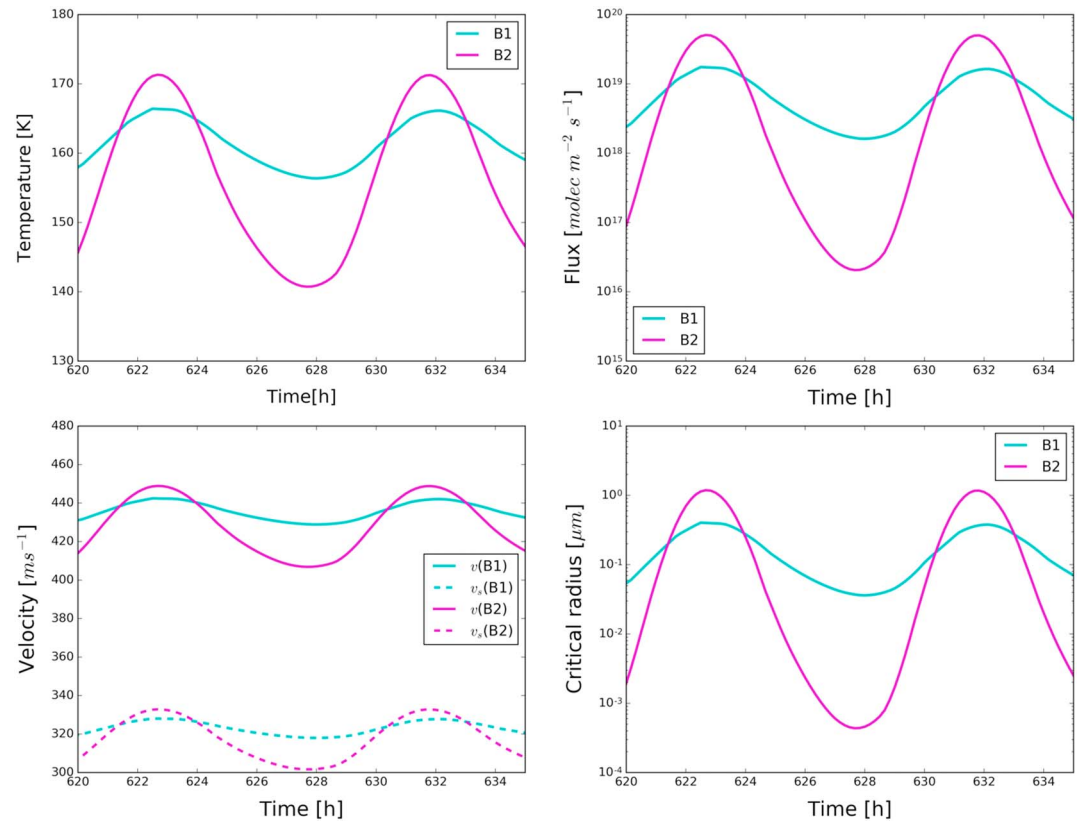


Figure 8. Characteristic behavior of the physical quantities for case B and for two different values of the thermal inertia: 500 TIU (case B1, cyan line) and 50 TIU (case B2, magenta line): (a) *Day-night* temperature profile in the icy region; (b) water flux in molecules $m^{-2} s^{-1}$; (c) velocity of the water vapor (v) and of the sound (v_s), where sound velocities are in dashed style; (d) critical radius for dust lifting.

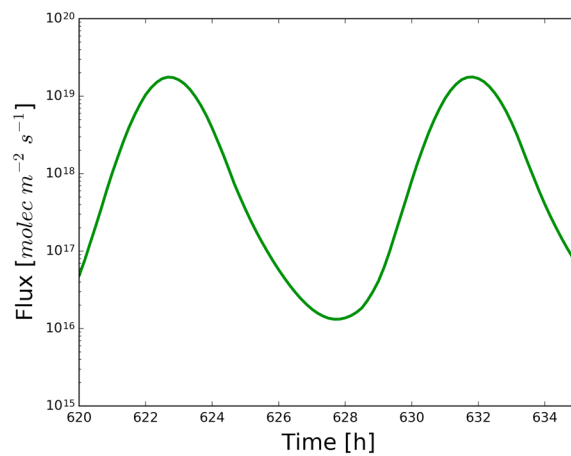


Figure 9. Flux versus time at heliocentric distance compatible with Herschel observations (Küppers et al., 2014), that is, 2.71 AU. Simulation is performed with an assumed thermal inertia of 50 TIU.

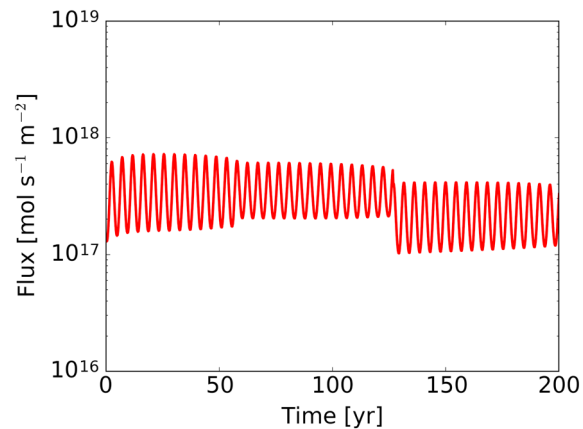


Figure 10. Flux versus time from the floor of the crater, in case of thermal inertia of 50 TIU, at 2.71 AU. We supposed that the ice layer was 1 cm deep.

4.2. Cases B: 2.55 AU—Perihelion

At the perihelion, the mean solar irradiance is about 50 W m^{-2} greater than the previous case, and it leads to a general increase of the mean temperature also in the “icy region”, now characterized by temperatures that can reach values $\approx 170 \text{ K}$ (see Figure 8a). If we calculate the emission rate according to equation (20), we obtain a maximum of $1.9 \times 10^{-2} \text{ mm}$ for rotation in B1, and $5.4 \times 10^{-2} \text{ mm}$ in B2. We note how the ice lifetime is now greatly reduced. Water fluxes are some orders of magnitudes greater than the previous case A (see Figure 8b), and also the velocity of the water vapor is now slightly greater (see Figure 8c). If we compute the maximum critical size for dust particle lifting we note that it is now $1 \mu\text{m}$ (Figure 8d), still smaller than the assumed typical grain size (Raponi et al., 2017).

4.3. Cases C and D : 2.71 AU—Herschel Comparison

The observations of the Herschel space observatory carried out in 2011–2013 (Küppers et al., 2014) suggested a water flux at least of $10^{26} \text{ molecules s}^{-1}$ by an area of 0.6 km^2 at mid latitude of Ceres. As pointed in Formisano, De Sanctis, et al. (2016), the ice on the surface of Ceres is in general very unstable (few orbits) at low latitudes, even if in the cited work we did not consider the topography and consequently the real illumination conditions. This result is also supported by Titus (2015). Conversely, the emission from a large subsurface area not very deep (compatible with the skin depth) is a likely scenario for the Herschel space observatory observations (Formisano, De Sanctis, et al., 2016).

Here we have calculated the flux emitted by the icy region (northern wall) of Juling at an heliocentric distance compatible with Herschel measurements (Küppers et al., 2014) (2.71 AU) and we can note that estimated flux does not match the Herschel measured value. In fact the computed average flux is $10^{18} \text{ molecules m}^{-2} \text{ s}^{-1}$ (see Figure 9) and the icy area is 40 km^2 , resulting in a different amount of water flux. These simulations are performed in case of thermal inertia equal to 50 TIU. However, the matching with Herschel observations could be reached if we consider an icy layer at a depth of 1 cm beneath the surface: in this case, the flux is about $10^{17} \text{ molecules m}^{-2} \text{ s}^{-1} - 10^{18} \text{ molecules m}^{-2} \text{ s}^{-1}$ (see Figure 10). By supposing that the whole floor of the crater (about 300 km^2) emits, the total flux would be close to the 6 kg s^{-1} of the Herschel estimation. Note

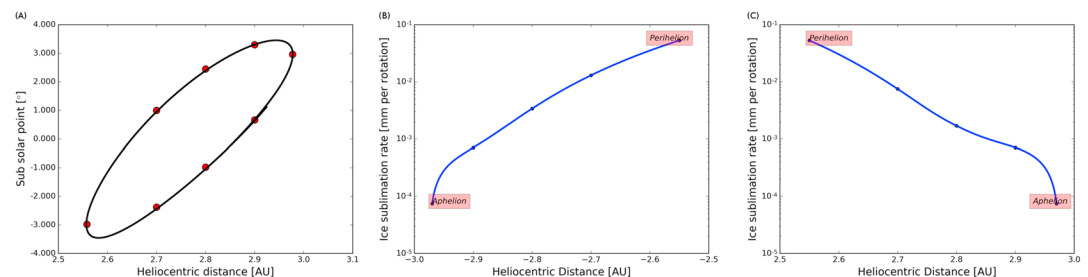


Figure 11. (a) Subsolar point evolution along the orbits, with red dots indicating the heliocentric distances under study; (b) ice erosion per rotation in preperihelion phase (indicated with a minus sign); (c) ice erosion per rotation in postperihelion phase. The evaluation is made for the case with thermal inertia at 50 TIU.

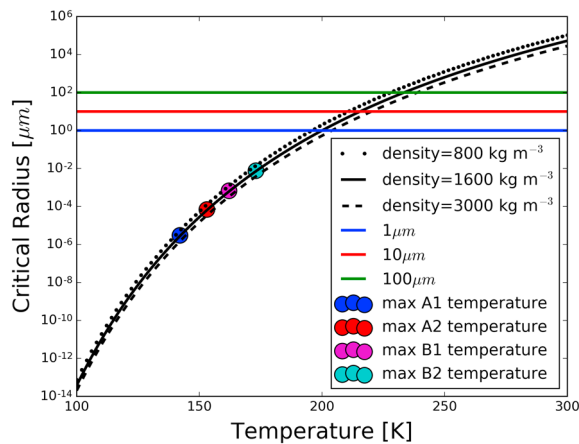


Figure 12. Critical radius size versus theoretical temperatures, ranging from 100 to 300 K. Horizontal lines correspond to different critical radii: in order to make possible the sublimation of a dust particle 100 μm in size, temperatures >230 K are needed, assuming three values for the dust density: 800, 1,600, and 3,000 kg m^{-3} .

temperature by using equation (26). We assume that the temperatures can reasonably range from 100 K to 300 K, values that can be compatible with a typical day-night cycle of a main belt asteroid. What we observe in Figure 12 is that, in order to make possible the lifting of dust particles of 100 μm in size, a surface temperature >230 K is required. However, assuming a typical lunar regolith density, that is, 1,600 kg m^{-3} (Heiken et al., 1991), these high temperatures are never reached in the icy region of the crater. The same calculation is done for low (800 kg m^{-3}) and high (3,000 kg m^{-3}) density values, obtaining very similar results, as shown in Figure 12.

The difficulty in lifting dust particles is also pointed out by Landis et al. (2017). In the physical parameters range they explore, they obtain critical radius of the order of tenth of microns or less. As a consequence, the lifting of the particles is not an efficient mechanism of exposure of “fresh” ice from the subsurface layers. It should be noted that Dawn’s Gamma Ray and Neutron Detector (GRaND) observations (Prettyman et al., 2017) are in a good agreement with the vapor diffusivity of a dust mantle with 1 μm particles, smaller than the typical lunar regolith particles (Heiken et al., 1991), making more likely the particle lifting. From Figure 12 we observe that particles lifting is possible at perihelion for low thermal inertia (case B2) if the size of the grain is 0.01 μm .

4.6. The Influence of the Hertz Factor

In order to evaluate the effects of the Hertz factor on the thermal history of our object, we now calculate the surface temperature assuming a Hertz factor equal to 1. In Figure 13 we report the new results

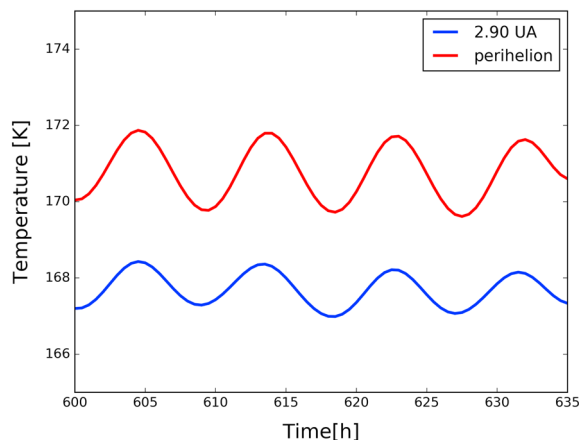


Figure 13. Temperature profile of the icy region for cases A and B with no Hertz factor effect. We note that the day-night curve is quite flat due to the high values of thermal inertia.

that a decrease in the flux starts after only about 50 yr and probably, in order to guarantee “fresh” ice on the superficial layers, a mechanism of refreshment, is needed. Juling could be the source (or one of the sources) of Herschel observations if we assume that all the crater is rich of ice and not only the icy northern wall, with the ice very close to the surface. Also this calculation was made for a thermal inertia of 50 TIU.

4.4. Ice Loss Along the Orbit

In order to give a suitable estimation of the ice loss along the orbit, we have calculated the maximum ice sublimation rate by using the equation (20) at specific heliocentric distances: perihelion, aphelion, 2.71 AU (pre and post perihelion), 2.80 AU (pre and post perihelion) and 2.90 AU (pre and post perihelion) as shown in Figure 11a, in which the subsolar point evolution is represented. We only focused on the case with thermal inertia of 50 TIU. In Figures 11b–11c we report the maximum ice loss for planetary rotation, by using equations (20) and (22), at different selected heliocentric distances. A spline interpolation is used. We observe a decrease of four orders of magnitude from perihelion to aphelion.

4.5. Critical Radius and Theoretical Temperature

We compute a theoretical profile of the critical radius as a function of the temperature by using equation (26). We assume that the temperatures can reasonably range from 100 K to 300 K, values that can be compatible with a typical day-night cycle of a main belt asteroid. What we observe in Figure 12 is that, in order to make possible the lifting of dust particles of 100 μm in size, a surface temperature >230 K is required. However, assuming a typical lunar regolith density, that is, 1,600 kg m^{-3} (Heiken et al., 1991), these high temperatures are never reached in the icy region of the crater. The same calculation is done for low (800 kg m^{-3}) and high (3,000 kg m^{-3}) density values, obtaining very similar results, as shown in Figure 12.

The difficulty in lifting dust particles is also pointed out by Landis et al. (2017). In the physical parameters range they explore, they obtain critical radius of the order of tenth of microns or less. As a consequence, the lifting of the particles is not an efficient mechanism of exposure of “fresh” ice from the subsurface layers. It should be noted that Dawn’s Gamma Ray and Neutron Detector (GRaND) observations (Prettyman et al., 2017) are in a good agreement with the vapor diffusivity of a dust mantle with 1 μm particles, smaller than the typical lunar regolith particles (Heiken et al., 1991), making more likely the particle lifting. From Figure 12 we observe that particles lifting is possible at perihelion for low thermal inertia (case B2) if the size of the grain is 0.01 μm .

In order to evaluate the effects of the Hertz factor on the thermal history of our object, we now calculate the surface temperature assuming a Hertz factor equal to 1. In Figure 13 we report the new results obtained for cases A and B: results refer to the ice-rich region. In both cases, the thermal conductivity is weighted on the assumed volumetric percentage of regolith and ice (10% in the shadow rim of the crater). The thermal inertia, in both case, exceeds 1,000 TIU and with this value the day-night profile is relatively “flat”, as shown in Figure 13, with oscillations of few kelvins. These plots suggest that a low value for the Hertz factor is crucial to recover the classical day-night temperature profile and also to obtain reasonable value of thermal inertia.

5. VIR Observations

VIR experimental data show that, at 2.961 AU distance at 9.4 hr local solar time (LAMO 1 - L1), the temperature of the icy wall is on average 160 ± 5 K (see Figure 14A). At 2.913 AU at 8.58 hr local solar time (LAMO 2 - L2), the ice wall has an average temperature of 162 ± 3 K (see Figure 14B). Note that the difference in the illumination conditions between L1 and L2 is very small since the mean solar irradiance

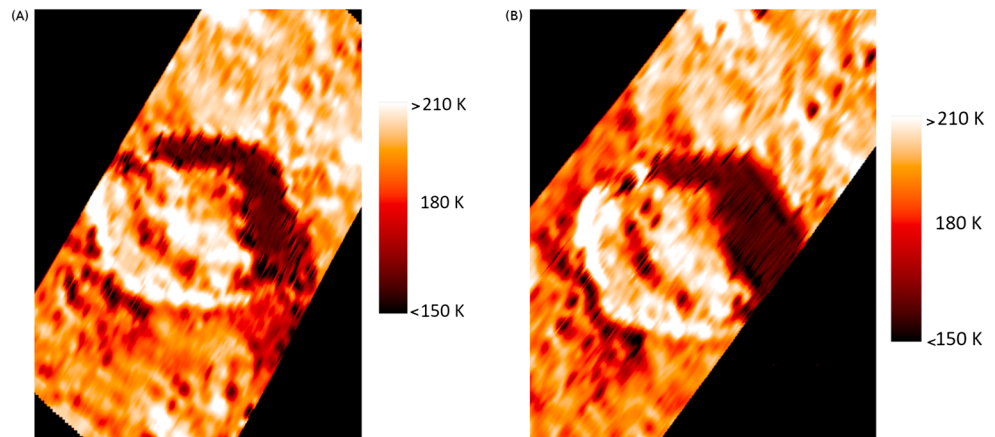


Figure 14. Temperature maps derived by VIR experimental data at (a) 2.961 AU at 9.4 hr local solar time (LAMO 1) and (b) 2.913 AU at 8.58 hr local solar time (LAMO 2). VIR = Visible and InfraRed mapping spectrometer.

changes of less than 10 W m^{-2} . In both case, the floor reaches high values: 222 K in L1 and 219 K in L2. The temperatures are derived with the same method discussed in Tosi et al. (2014).

The comparison with our numerical results show a good agreement in case of low thermal inertia (50 TIU): the ice-rich region reaches a maximum temperature of 150 K while the floor a maximum temperature of 210 K. In case of high thermal inertia (500 TIU), our simulated temperatures are quite different: the icy wall reaches a maximum temperature of 140 K while the floor 190 K.

6. Conclusions

In this work, having applied a 3-D FEM code, we studied the surface temperature and the water ice sublimation in a specific region of the dwarf planet Ceres, namely the Juling crater, one of the few locations where water ice has been detected by VIR (Raponi et al., 2018). Our analysis was carried out at varying heliocentric distances and under different thermophysical assumptions. Our simulations have shown that the crater's northern rim and inner wall, where ice has been detected, are poorly illuminated at heliocentric distances compatible with VIR observations (Raponi et al., 2018), i.e. 2.90 AU. Such illumination conditions lead to relatively low surface temperatures ($<150 \text{ K}$), while the floor of the crater reaches a temperature $<210 \text{ K}$ and, consequently, a low water flux ($< 10^{18} \text{ molecules m}^{-2} \text{ s}^{-1}$ along the rim) has been estimated. Conversely, at the perihelion, the icy region reaches a temperature as high as 170 K and the water flux is increased of about two orders of magnitude.

One of our simulations has been also performed at roughly the same heliocentric distance at which Herschel space observatory first detected water vapor on Ceres (Küppers et al., 2014), 2.71 AU, obtaining an average water flux of $10^{18} \text{ molecules m}^{-2} \text{ s}^{-1}$ in the case of thermal inertia of 50 TIU: the estimated flux value is not consistent with Herschel observations since it would require a larger area than the icy wall (40 km^2). Instead, assuming that the ice is present in the crater's floor at a depth of 1 cm, compatible with the diurnal skin depth, the cross-out flux will be between $10^{17} \text{ molecules m}^{-2} \text{ s}^{-1}$ and $10^{18} \text{ molecules m}^{-2} \text{ s}^{-1}$. Assuming that whole floor (whose mean radius is 10 km) contributes to the water ice flux, we will get a water flux very close to the 6 kg s^{-1} estimated by Herschel. However, this ice will be stable for a short period at a depth of 1 cm and a continuous replenishment will be essential. Under these premises, Juling could represent the source of the Herschel observations if we assume that both the floor and the ice-rich northern wall of the crater can contribute to the water vapor emission. The application of the simplified theory on the lifting of dust particles, developed in section 3.2, shows that the lifting of particles $100 \mu\text{m}$ in size (Raponi et al., 2017) is possible with high temperatures ($>230 \text{ K}$, slightly dependent on the density), which probably are reached only at perihelion for short daytime periods. However, in the northern inner wall the sublimation can "detach" the dust particle from the ice creating micro-landslides that could be responsible of the exposure of fresh ice if this is mantled by a dust blanket.

As discussed in Raponi et al. (2018), the northern wall of the crater shows signatures of water ice. The water ice content has changed during the six months of observations from April 2016 to October 2016. An increase of the water ice content is observed, which seems to be correlated with the solar flux. In particular, it is hypothesized that water vapor might originate from the hot floor and accumulate over the cold northern wall. According to Raponi et al. (2018), at that time we were probably observing the “increasing part” of a general complete season cycle of water sublimation and condensation. In this context, our work seems to confirm that (1) the northern wall of the crater is faintly illuminated along the orbit; 2) a variability of the sublimation rate along the orbit.

By comparing our simulated temperature with those derived by VIR experimental data, we observe that the simulations give a good agreement with the VIR derived temperatures in case of low thermal inertia, that is, 50 TIU. In fact, both in L1 and L2, the ice-rich region reaches maximum temperatures that are compatible with our numerical predictions. In case of the floor, the difference between VIR and simulated temperatures is slightly greater than 5%. The evidence that the VIR derived temperatures are slightly higher than the modeled ones may depend on the fact that the re-emitted energy here is not computed in the energy balance.

This comparison seems to indicate that the surface could be characterized by low (less than 50 TIU) thermal inertia, which implies a low thermal conductivity. In this sense, the role of the Hertz factor seems to be crucial to reduce the thermal conductivity and also to reduce the day-night temperature oscillations.

Our result indicate that the faint solar illumination makes the northern wall of Juling crater a good place to host water ice on the surface of Ceres.

Acknowledgments

This work is supported by an ASI (Agenzia Spaziale Italiana) grant. Numerical output tables and digital terrain model (DTM) converted in a stereolithography (STL) file are available at <https://github.com/MiFormisano/miformisano>. We would like to thank T. N. Titus and M. Landis for their useful comments and suggestions which largely improved the clarity of our manuscript.

References

- A'Hearn, M. F., & Feldman, P. D. (1992). Water vaporization on Ceres. *Icarus*, 98, 54–60. [https://doi.org/10.1016/0019-1035\(92\)90206-M](https://doi.org/10.1016/0019-1035(92)90206-M)
- Bland, M. T., Raymond, C. A., Schenk, P. M., Fu, R. R., Kneissl, T., Pasckert, J. H., et al. (2016). Composition and structure of the shallow subsurface of Ceres revealed by crater morphology. *Nature Geoscience*, 9, 538–542. <https://doi.org/10.1038/ngeo2743>
- Capria, M. T., Capaccioni, F., Coradini, A., De Sanctis, M. C., Espinasse, S., Federico, C., et al. (1996). A P/Wirtanen evolution model. *Planetary and Space Science*, 44, 987–1000. [https://doi.org/10.1016/0032-0633\(96\)00016-5](https://doi.org/10.1016/0032-0633(96)00016-5)
- Carrozzo, F. G., De Sanctis, M. C., Raponi, A., Ammannito, E., Castillo-Rogez, J., Ehlmann, B. L., et al. (2018). Nature, formation, and distribution of carbonates on Ceres. *Science Advances*, 4(3). <https://doi.org/10.1126/sciadv.1701645>
- Castillo-Rogez, J. C. (2011). Ceres—Neither a porous nor salty ball. *Icarus*, 215, 599–602. <https://doi.org/10.1016/j.icarus.2011.08.007>
- Castillo-Rogez, J. C., & McCord, T. B. (2010). Ceres' evolution and present state constrained by shape data. *Icarus*, 205, 443–459. <https://doi.org/10.1016/j.icarus.2009.04.008>
- Chamberlain, M. A., Sykes, M. V., & Esquerdo, G. A. (2007). Ceres lightcurve analysis-period determination. *Icarus*, 188(2), 451–456. <https://doi.org/10.1016/j.icarus.2006.11.025>
- Ciarniello, M., De Sanctis, M. C., Ammannito, E., Raponi, A., Longobardo, A., Palomba, E., et al. (2017). Spectrophotometric properties of dwarf planet Ceres from the VIR spectrometer on board the Dawn mission. *A & A*, 598, A130. <https://doi.org/10.1051/0004-6361/201629490>
- Clark, R. N., Cruikshank, D. P., Jaumann, R., Brown, R. H., Stephan, K., Ore, C. M. D., et al. (2012). The surface composition of Iapetus: Mapping results from Cassini VIMS. *Icarus*, 218(2), 831–860. <https://doi.org/10.1016/j.icarus.2012.01.008>
- Combe, J.-P., McCord, T. B., Tosi, F., Ammannito, E., Carrozzo, F. G., De Sanctis, M. C., et al. (2016). Detection of local H₂O exposed at the surface of Ceres. *Science*, 353, aaf3010. <https://doi.org/10.1126/science.aaf3010>
- De Sanctis, M. C., Ammannito, E., Raponi, A., Marchi, S., McCord, T. B., McSween, H. Y., et al. (2015). Ammoniated phyllosilicates with a likely outer solar system origin on (1) Ceres. *Nature*, 528, 241–244. <https://doi.org/10.1038/nature16172>
- De Sanctis, M. C., Coradini, A., Ammannito, E., Filacchione, G., Capria, M. T., Fonte, S., et al. (2011). The VIR spectrometer. *Space Science Reviews*, 163, 329–369. <https://doi.org/10.1007/s11214-010-9668-5>
- De Sanctis, M. C., Raponi, A., Ammannito, E., Ciarniello, M., Toplis, M. J., McSween, H. Y., et al. (2016). Bright carbonate deposits as evidence of aqueous alteration on (1) Ceres. *Nature*, 536, 54–57. <https://doi.org/10.1038/nature16172>
- De Sanctis, M. C., Lasue, J., & Capria, M. T. (2010). Seasonal effects on comet nuclei evolution: Activity, internal structure, and dust mantle formation. *The Astronomical Journal*, 140, 1–13. <https://doi.org/10.1088/0004-6256/140/1/1>
- De Sanctis, M. C., Lasue, J., Capria, M. T., Magni, G., Turrini, D., & Coradini, A. (2010). Shape and obliquity effects on the thermal evolution of the Rosetta target 67P/Churyumov-Gerasimenko cometary nucleus. *Icarus*, 207, 341–358. <https://doi.org/10.1016/j.icarus.2009.11.009>
- Delsemme, A. H., & Miller, D. C. (1971). The continuum of Comet Burnham (1960 II): The differentiation of a short period comet. *Planetary and Space Science*, 19, 1229–1257. [https://doi.org/10.1016/0032-0633\(71\)90180-2](https://doi.org/10.1016/0032-0633(71)90180-2)
- Ellsworth, K., & Schubert, G. (1983). Saturn's icy satellites—Thermal and structural models. *Icarus*, 54, 490–510. [https://doi.org/10.1016/0019-1035\(83\)90242-7](https://doi.org/10.1016/0019-1035(83)90242-7)
- Espinasse, S., Klinger, J., Ritz, C., & Schmitt, B. (1991). Modeling of the thermal behavior and of the chemical differentiation of cometary nuclei. *Icarus*, 92, 350–365. [https://doi.org/10.1016/0019-1035\(91\)90058-2](https://doi.org/10.1016/0019-1035(91)90058-2)
- Fanale, F. P., & Salvail, J. R. (1984). An idealized short-period comet model—Surface insolation, H₂O flux, dust flux, and mantle evolution. *Icarus*, 60, 476–511. [https://doi.org/10.1016/00191035\(84\)90157-X](https://doi.org/10.1016/00191035(84)90157-X)
- Fanale, F. P., & Salvail, J. R. (1987). The loss and depth of CO₂ ice in comet nuclei. *Icarus*, 72, 535–554. [https://doi.org/10.1016/0019-1035\(87\)90051-0](https://doi.org/10.1016/0019-1035(87)90051-0)
- Fanale, F. P., & Salvail, J. R. (1989). The water regime of asteroid (1) Ceres. *Icarus*, 82, 97–110. [https://doi.org/10.1016/0019-1035\(89\)90026-2](https://doi.org/10.1016/0019-1035(89)90026-2)
- Formisano, M., De Sanctis, M. C., Magni, G., Federico, C., & Capria, M. T. (2016). Ceres water regime: Surface temperature, water sublimation and transient exo(atmo)sphere. *MNRAS*, 455, 1892–1904. <https://doi.org/10.1093/mnras/stv2344>

- Formisano, M., Federico, C., De Angelis, S., De Sanctis, M. C., & Magni, G. (2016). The stability of the crust of the dwarf planet Ceres. *MNRAS*, 463, 520–528. <https://doi.org/10.1093/mnras/stw1910>
- Fu, R. R., Ermakov, A. I., Marchi, S., Castillo-Rogez, J. C., Raymond, C. A., Hager, B. H., et al. (2017). The interior structure of Ceres as revealed by surface topography. *Earth and Planetary Science Letters*, 476(Supplement C), 153–164. <https://doi.org/10.1016/j.epsl.2017.07.053>
- Hapke, B. (2012). *Theory of Reflectance and Emission Spectroscopy* (2nd ed.). Cambridge, UK: Cambridge University Press. <https://doi.org/10.1017/CBO9781139025683>
- Hayne, P. O., & Aharonson, O. (2015). Thermal stability of ice on Ceres with rough topography. *Journal of Geophysical Research: Planets*, 120, 1567–1584. <https://doi.org/10.1002/2015JE004887>
- Heiken, G. H., Vaniman, D. T., & French, B. M. (1991). Lunar sourcebook—A user's guide to the Moon.
- Hudgins, D. M., Sandford, S. A., Allamandola, L. J., & Tielens, A. G. G. M. (1993). Mid- and far-infrared spectroscopy of ices—Optical constants and integrated absorbances. *The Astrophysical Journal Supplement Series*, 86, 713–870. <https://doi.org/10.1086/191796>
- Huebner, W. F. (2006). *Heat and Gas Diffusion in Comet Nuclei*, ISSI scientific report: International Space Science Institute. Noordwijk, Netherlands: ESA, Publications Division.
- Keihm, S., Kamp, L., Gulkis, S., Hofstadter, M., Lee, S., Janssen, M., & Choukroun, M. (2013). Reconciling main belt asteroid spectral flux density measurements with a self-consistent thermophysical model. *Icarus*, 226, 1086–1102. <https://doi.org/10.1016/j.icarus.2013.07.005>
- Klinger, J. (1980). Influence of a phase transition of ice on the heat and mass balance of comets. *Science*, 209, 271. <https://doi.org/10.1126/science.209.4453.271>
- Koemle, N. I., Steiner, G., Seidensticker, K. J., Kochan, H., Thomas, H., Thiel, K., et al. (1992). Temperature evolution and vapour pressure build-up in porous ices. *Planetary and Space Science*, 40, 1311–1323. [https://doi.org/10.1016/0032-0633\(92\)90088-6](https://doi.org/10.1016/0032-0633(92)90088-6)
- Kossacki, K. J., Koinle, N. I., Kargl, G., & Steiner, G. (1994). The influence of grain sintering on the thermoconductivity of porous ice. *Planetary and Space Science*, 42(5), 383–389. [https://doi.org/10.1016/0032-0633\(94\)90127-9](https://doi.org/10.1016/0032-0633(94)90127-9)
- Küppers, M., O'Rourke, L., Bockelée-Morvan, D., Zakharov, V., Lee, S., von Allmen, P., et al. (2014). Localized sources of water vapour on the dwarf planet (1)Ceres. *Nature*, 505, 525–527. <https://doi.org/10.1038/nature12918>
- Landis, M. E., Byrne, S., Schörghofer, N., Schmidt, B. E., Hayne, P. O., Castillo-Rogez, J., et al. (2017). Conditions for sublimating water ice to supply Ceres' exosphere. *Journal of Geophysical Research: Planets*, 122, 1984–1995. <https://doi.org/10.1002/2017JE005335>
- Lasue, J., De Sanctis, M. C., Coradini, A., Magni, G., Capria, M. T., Turrini, D., et al. (2008). Quasi-3-D model to describe topographic effects on non-spherical comet nucleus evolution. *Planetary and Space Science*, 56, 1977–1991. <https://doi.org/10.1016/j.pss.2008.08.020>
- Li, J.-Y., Reddy, V., Nathues, A., Le Corre, L., Izawa, M. R. M., Cloutis, E. A., et al. (2016). Surface albedo and spectral variability of Ceres. *The Astrophysical Journal Letters*, 817, L22. <https://doi.org/10.3847/2041-8205/817/2/L22>
- Marchi, S., Ermakov, A. I., Raymond, C. A., Fu, R. R., O'Brien, D. P., Bland, M. T., et al. (2016). The missing large impact craters on Ceres. *Nature Communications*, 7, 12257. <https://doi.org/10.1038/ncomms12257>
- McCord, T. B., & Sotin, C. (2005). Ceres: Evolution and current state. *Journal of Geophysical Research*, 110, 5009. <https://doi.org/10.1029/2004JE002244>
- McKinnon, W. B. (2008). On the possibility of large KBOs being injected into the outer asteroid belt, Aas/Division for planetary sciences meeting abstracts #40. *Bulletin of the American Astronomical Society*, 40, 464.
- Mellon, M. T., Feldman, W. C., & Prettyman, T. H. (2004). The presence and stability of ground ice in the southern hemisphere of Mars. *Icarus*, 169(2), 324–340. <https://doi.org/10.1016/j.icarus.2003.10.022>
- Murphy, D. M., & Koop, T. (2005). Review of the vapour pressures of ice and supercooled water for atmospheric applications. *Quarterly Journal of the Royal Meteorological Society*, 131(608), 1539–1565. <https://doi.org/10.1256/qj.04.94>
- Nathues, A., Hoffman, M., Schaefer, M., Le Corre, L., Reddy, V., Platz, T., et al. (2015). Sublimation in bright spots on (1) Ceres. *Nature*, 528, 237–240. <https://doi.org/10.1038/nature15754>
- Neveu, M., & Desch, S. J. (2015). Geochemistry, thermal evolution, and cryovolcanism on Ceres with a muddy ice mantle. *Geophysical Research Letters*, 42, 10. <https://doi.org/10.1002/2015GL066375>
- Neveu, M., Desch, S. J., & Castillo-Rogez, J. C. (2015). Core cracking and hydrothermal circulation can profoundly affect Ceres' geophysical evolution. *Journal of Geophysical Research: Planets*, 120, 123–154. <https://doi.org/10.1002/2014JE004714>
- Park, R. S., Konopliv, A. S., Bills, B., Castillo-Rogez, J., Asmar, S. W., Rambaux, N., et al. (2016). Gravity science investigation of Ceres from Dawn. In *Lunar and planetary science conference, Lunar and Planetary Science Conference*, pp. 1781.
- Paton, M. D., Kargl, G., Ball, A. J., Green, S. F., Hagermann, A., Kömle, N. I., et al. (2010). Computer modelling of a penetrator thermal sensor. *Advances in Space Research*, 46(3), 337–345. <https://doi.org/10.1016/j.asr.2010.03.007>
- Prettyman, T. H., Yamashita, N., Toplis, M. J., McSween, H. Y., Schörghofer, N., Marchi, S., et al. (2017). Extensive water ice within Ceres' aqueously altered regolith: Evidence from nuclear spectroscopy. *Science*, 355, 55–59. <https://doi.org/10.1126/science.aah6765>
- Preusker, F., Scholten, F., Matz, K.-D., Elgner, S., Jaumann, R., Roatsch, T., et al. (2016). Dawn at Ceres: Shape model and rotational state. In *Lunar and planetary science conference, Lunar and Planetary Science Conference*, 47, pp. 1954.
- Raponi, A., Carrozzo, F. G., Zambon, F., Sanctis, M. C. D., Ciarniello, M., Frigeri, A., et al. (2017). Mineralogical mapping of Coniraya quadrangle of the dwarf planet Ceres. *Icarus*, 4. <https://doi.org/10.1016/j.icarus.2017.10.023>
- Raponi, A., De Sanctis, M. C., Frigeri, A., Ammannito, E., Ciarniello, M., Formisano, M., et al. (2018). Variations in the amount of water ice on Ceres' surface suggest a seasonal water cycle. *Science Advances*, 4(3), eaao3757. <https://doi.org/10.1126/sciadv.aao3757>
- Rivkin, A. S., Li, J.-Y., Milliken, R. E., Lim, L. F., Lovell, A. J., Schmidt, B. E., et al. (2011). The surface composition of Ceres. *Space Science Reviews*, 163, 95–116. <https://doi.org/10.1007/s11214-010-9677-4>
- Roth, L., Ivchenko, N., Retherford, K. D., Cunningham, N. J., Feldman, P. D., Saur, J., et al. (2016). Constraints on an exosphere at Ceres from Hubble Space Telescope observations. *Geophysical Research Letters*, 43(6), 2465–2472. <https://doi.org/10.1029/2015GL067451>
- Ruesch, O., Platz, T., Schenk, P., McFadden, L. A., Castillo-Rogez, J. C., Quick, L. C., et al. (2016). Cryovolcanism on Ceres. *Science*, 353, aaf4286. <https://doi.org/10.1126/science.aaf4286>
- Russell, C. T., Raymond, C. A., Ammannito, E., Buczkowski, D. L., De Sanctis, M. C., Hiesinger, H., et al. (2016). Dawn arrives at Ceres: Exploration of a small, volatile-rich world. *Science*, 353, 1008–010. <https://doi.org/10.1126/science.aaf4219>
- Schmidt, B. E., Hughson, K. H. G., Chilton, H. T., Scully, J. E. C., Platz, T., Nathues, A., et al. (2017). Geomorphological evidence for ground ice on dwarf planet Ceres. *Nature Geoscience*, 10, 338–343. <https://doi.org/10.1038/ngeo2936>
- Schorghofer, N., Mazarico, E., Platz, T., Preusker, F., Schröder, S. E., Raymond, C. A., et al. (2016). The permanently shadowed regions of dwarf planet Ceres. *Geophysical Research Letters*, 43, 6783–6789. <https://doi.org/10.1029/2016GL069368>
- Sierks, H., Keller, H. U., Jaumann, R., Michalik, H., Behnke, T., Bubenhausen, F., et al. (2011). The Dawn Framing Camera. *Space Science Reviews*, 163, 263–327. <https://doi.org/10.1007/s11214-011-9745-4>
- Spencer, J. R., Lebofsky, L. A., & Sykes, M. V. (1989). Systematic biases in radiometric diameter determinations. *Icarus*, 78, 337–354. [https://doi.org/10.1016/0019-1035\(89\)90182-6](https://doi.org/10.1016/0019-1035(89)90182-6)

- Titus, T. N. (2015). Ceres: Predictions for near-surface water ice stability and implications for plume generating processes. *Journal of Geophysical Research: Planets*, 42, 2130–2136. <https://doi.org/10.1002/2015GL063240>
- Tosi, F., Capria, M. T., Sanctis, M. C. De, Combe, J.-Ph., Zambon, F., Nathues, A., et al. (2014). Thermal measurements of dark and bright surface features on Vesta as derived from Dawn/VIR. *Icarus*, 240, 36–57. <https://doi.org/10.1016/j.icarus.2014.03.017>
- Tosi, F., Carozzo, F. G., Zambon, F., Ciarniello, M., Frigeri, A., Combe, J.-Ph., et al. (2017). Mineralogical analysis of the Ac-H-6 Haulani quadrangle of the dwarf planet Ceres. *Icarus*, 1–18. <https://doi.org/10.1016/j.icarus.2017.08.012>
- Villarreal, M. N., Russell, C. T., Luhmann, J. G., Thompson, W. T., Prettyman, T. H., A'Hearn, M. F., et al. (2017). The dependence of the Cerean exosphere on solar energetic particle events. *The Astrophysical Journal Letters*, 838(1), L8.
- Zolotov, M. Y. (2017). Aqueous origins of bright salt deposits on Ceres. *Icarus*, 296, 289–304. <https://doi.org/10.1016/j.icarus.2009.06.011>